08

Theoretical and experimental studies of micromagnets for a silicon quantum processor

© O.L. Ermolaeva,[1] E.V. Skorokhodov,[1] R.V. Gorev,[1] E.V. Demidov,[1] S.V. Sitnikov,[2] D.A. Nasimov,[2] M.V. Sapozhnikov[1,3]

[1]Institute of Physics of Microstructures, Russian Academy of Sciences,
603087 Afonino, Kstovsky District, Nizhny Novgorod Oblast, Russia
[2]Rzhanov Institute of Semiconductor Physics, Siberian Branch, Russian Academy of Sciences,
630090 Novosibirsk, Russia
[3]Lobachevsky State University,
603022 Nizhny Novgorod, Russia
e-mail: ermolaeva@ipmras.ru

Received April 27, 2024
Revised April 27, 2024
Accepted April 27, 2024

The paper describes the experimental and numerical investigations of micromagnets designed for inhomogeneous field generation in silicon qubits based on Si/SiGe heterostructures with quantum dots formed by electric gates. Measurements were performed by the optical magnetometry and magnetic force microscopy methods. It is shown that the given micromagnet geometry ensures magnetic field gradients required to induce the electric dipole spin resonance in one or more quantum dots and is suitable to control qubit states based on quantum dots.

Keywords: micromagnets, quantum dots, qubits, cobalt films.

DOI: 10.61011/TP.2024.07.58803.146-24

Introduction

Currently, quantum computers and quantum computations are being extended from the fundamental research domain into the area of practical applications [1]. Creation of quantum computers to be used in the existing data processing centers for solution of specific tasks was reported [2]. Including computers with more than 1000 qubits [3]. All this results in fast growth of the quantum calculation market [4]. The reported progress in the utilization of quantum computers is associated with superconducting qubits and qubits based on ions or neutral atoms. These types of computers will probably take the lead in the quantum computation area in the near-term and mid-term period. However, all reported material platforms have one serious disadvantage coming from a problem of scalability of a general-purpose quantum computer that requires up to 1 000 000 qubits. At this point, semiconductor qubits are supposed to have no this disadvantage [5].

Although semiconductor qubit computers are yetfar below superconductor and „atomic“ computers in the number of the used qubits, they have shown a very fast advance in development that is mainly attributed to the evolvement of qubit formation techniques using silicon and silicon heterostructures with germanium [6]. The most significant achievements in the semiconductor qubit area over recent years include:

— achievement of two-qubit operation accuracy sufficient for employment of an error-correcting surface code [7–9];

— demonstration of 16-qubit system with address interaction between neighboring qubits [10];

— transit from qubit production in research laboratories to commercial production [11,12];

— fabrication of the first commercial semiconductor quantum processor [13].

Note that these findings have been demonstrated on four various types of qubits using nuclear spin of phosphorus isotope 31P in silicon [9], qubits based on electron spin manipulation in Si MOS structures [11,13] and Si/SiGe [7,8] structures, and qubits based on hole spin manipulation in Ge/SiGe [10] structures. Each of these types of qubits is characterized by its own set of advantages and disadvantages [6,12]. In this line, qubits based on Si/SiGe heterostructures are characterized by a low noise level to ensure the achievement of high accuracy of two-qubit operations for them [7,8]. Low noise level in this type of qubits is ensured by:

— low content of isotopes with non-zero nuclear spin due to the use of sources based on isotopically-enriched ^{28}Si for structure formation;

— high quality of formed structures that may be characterized by mobility of electrons in the Si quantum well;

— epitaxial SiGe layer separating the electron localization region from amorphous dielectric layers that are the main source of charge noise;

— weak spin-orbit interaction of electrons in the SiGe structures.

The latter requires either electron paramagnetic resonance (EPR) or electric dipole spin resonance (EDSR) for electron spin control [14]. EPR was used primarily at early stages of qubit generation efforts. EPR's disadvantage is in the fact that it needs variable magnetic field that is formed for

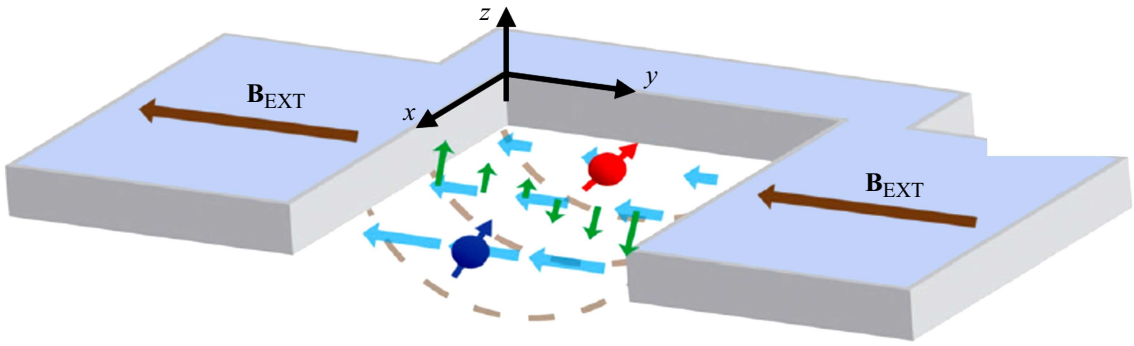

Figure 1. Example of micromagnet design showing magnetic field components in various directions. Blue and red circles with arrows show schematically two QD generation location. $\mathbf{B}_{\mathrm{EXT}}$ — constant magnetic field from external magnet. Blue and green arrows show z and y components of field $\mathbf{B}$.

by AC flow through the strip line, which is associated with additional heat release. Moreover, it is difficult to implement targeted control using EPR in systems with many qubits. Therefore, recent studies more often use EDSR for electron spin manipulation in the Si/SiGe qubits. The essence of the approach is in spin transition between the Zeeman energy levels that occurs when the quantum dot (QD) is shifted by electric voltage applied to one of the control electrodes in spatially inhomogeneous magnetic field. Thus, for EDSR implementation, a magnetic field gradient and AC voltage supply to control gates are needed [15]. Micro- and nanomagnets placed in various layers of the formed structure are used in the desired direction to create a magnetic field gradient [14,15]. Design and parameters of micro- and nanomagnets define to a great extent quick response of the systems and have considerable influence on the electron spin coherency time [14].

Example of a micromagnet placed above all control electrode layers and separated from them by a thin dielectric layer is shown in Figure 1. It consists of two strips connected by a bar that serves to create an inhomogeneous field in the micromagnet gap. Micromagnet is usually placed above the upper layer of electrodes and is separated from them by a thin dielectric layer ~ 100 nm. Review of the literature [14,15] shows that the use of micromagnets is currently most advantageous for creation of inhomogeneous Zeeman spin-splitting of electrons in neighboring quantum dots for EDSR implementation.

The Zeeman splitting of electron states with various spin orientation is defined by the sum of magnetic field components in direction y from the external constant magnet B_{EXT} and micromagnet B_y. inhomogeneous magnetic field component in direction z $(\mathbf{B}_z)$ shown by green arrows in Figure 1 is induced by the micromagnet and depends on its parameters and design. When the variable electric field in introduced, the wave function peak of an electron localized in QD shifts in direction y. And due to the presence of field gradient dBZ/dy, the electron is exposed to the variable magnetic field perpendicular to direction y that results in resonance transitions between the electron states with various spin directions. Micromagnet design shown in Figure 1 enables independent control of spin states in various QD. Such possibility arises from noniniform distribution of the magnetic field strength $\mathbf{B}_y$ (blue arrows) in the micromagnet along direction x.

However, note that QD shift in plane (x, y) by electric potential fluctuations induced, for example, by deep center recharging at the semiconductor —dielectric interface will also result in variation of the magnetic field component B_y and, therefore, to Zeeman splitting variation and spin state dephasing. Therefore, magnetic field gradients of the micromagnets make the spin states sensitive to electric noises and limit their coherency time: This negative effect may be minimized by selecting the best micromagnet design.

The study involves experimental investigations of micromagnets with high spatial resolution and calculations of distribution of their magnetic field aimed at optimization of the micromagnet design in order to increase the qubit response rate and the phase coherency time.

1. Samples and methods of investigation

The test micromagnets were fabricated by the Institute of Semiconductor Physics, Siberian Branch, Russian Academy of Sciences, by the „lift-off“ lithography using Raith lithography tool from 200 nm cobalt film formed by the magnetron sputtering method. A 400 nm electron-beam resist (PMMA) was used for magnet fabrication. Micromagnets are composed of two strips interconnected by a Π-shaped bridge (Figure 2).

The specimens were made on two types of wafers. A silicon wafer was used to form structures for magnetic field gradient measurement around micromagnets by a magnetic atomic-force microscope (Figure 2, a).

To measure the magneto-optic Kerr effect, a micromagnet array was made on an optically transparent material — SiO2 with Al_2O_3 sunlayer (Figure 2, b). To prevent the accumulation of surface charge resulting in pattern distortion, an additional 12–15 nm aluminum layer was

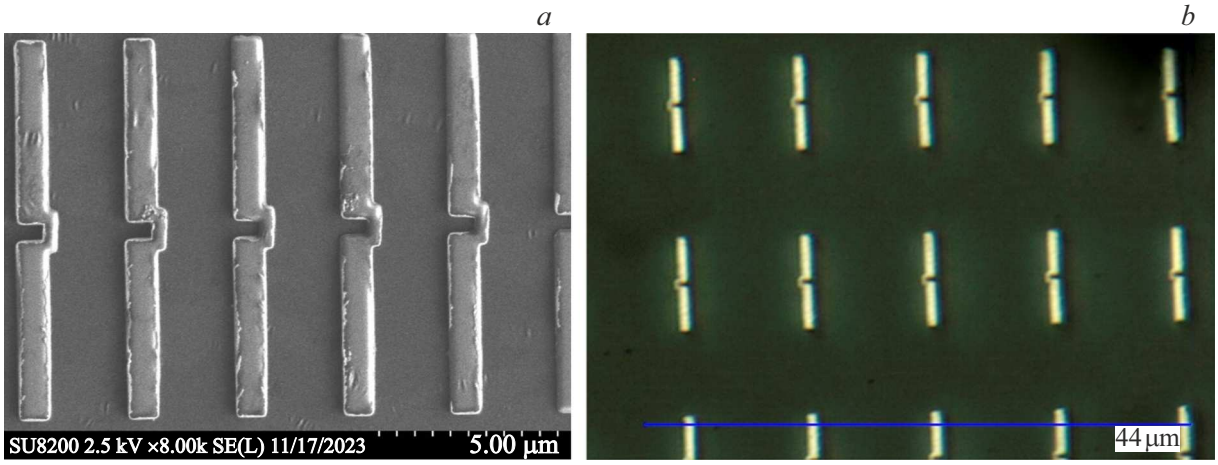

Figure 2. *a* — SEM image of Si-wafer micromagnet array for MFM measurements, *b* — optical microscope image of the SiO2-wafer micromagnet array examined by the optical magnetometry methods.

deposited n the electron-beam resist surface. The aluminum layer makes it possible to remove the charge from the surface and achieve a good resist pattern on the SiO2 surface. Before the development of the electron-beam resist, aluminum was removed using nitrogen acid. Then 200 nm Co with 10 nm Ti sublayer was deposited and lift-off lithography was performed.

Experimental examinations of the micromagnets were performed using two methods. The magnetization loop was measured by the optical magnetometry method with measurement of the magneto-optic Kerr effect in meridional geometry with crossed polarizer configuration. Stabilized (power stabilization 0.1% per min) He−Ne laser at a wavelength of 632 nm was used as the radiation source. To increase the signal, arrays of the same micromagnets, rather than single micromagnets, were examined (Figure 2, *b*).

Magnetic field distribution from a single micromagnet was examined by the magnetic force microscopy (MFM) method using Solver HV microscope. This microscope was equipped with a magnet used to produce a constant magnetic field up to 0.5 T in the specimen plane. The measurements were performed both with and without the magnetic field.

To study the magnetic properties of micromagnets, a two-pass MFM scanning technique was used [16]. The height of the second probe pass was 800 nm, which is sufficient to obtain an MFM image with adequate resolution avoiding the negative effect of the specimen topography. The MFM measurements were performed in 10^{-4} Torr vacuum, and, thus, the microscope sensitivity was increased considerably due to the increase in the cantilever Q factor up to $Q = 800$.

For experimental findings analysis, numerical simulation was used. The micromagnetic simulation used numerical solution of the Landau−Lifshitz−Hilbert equation in MuMax3 package [17]. The calculations used the following constitutive parameters of cobalt: saturation magnetization $1.4 \cdot 10^6$ A/m, exchange interaction constant $30 \cdot 10^{-12}$ J/m. For faster magnetization relaxation to equilibrium state and count time reduction, the decay parameter equal to 0.5 was chosen. Rectangular $128 \times 1024 \times 32$ mesh grid was used for simulation. The MFM microscope probe for calculations of the MFM images was assumed as a point dipole magnetized perpendicular to the specimen plane.

2. Findings and discussion

The magnetization loop experimentally measured by the optical magnetometry method is shown in Figure 3, *a*. The magnetic field was applied along the micromagnets. Since the degree of surface filling with the magnetic material in the micromagnet grid is very low ($\sim 5\%$), the magnetization loop was averaged with respect to 100 passes to increase the signal-to-noise ratio. The measured hysteresis loop width is 6.4 mT. The measured hysteresis loop was compared with the hysteresis loop calculated by means of the micromagnet simulation. The hysteresis loop width obtained by means of simulation was equal to 10 mT (Figure 3, *b*, red curve), which is much higher than the experimentally measured width. The saturation field is within 10−15 mT. Such discrepancy, according to out opinion, may be explained by two factors.

The first possible reason is that the test specimens have different geometrical defects and inhomogeneous internal structure because they are a polycrystal. This simplifies the remagnetization process associated with magnetic vortex (domain wall) inlet and outlet in the micromagnet.

The second possible factor — is the overestimated saturation magnetization used for the simulation and equal to $1.4 \cdot 10^6$ A/m, which corresponds to the bulk material. To match the experimental curve with the simulation results during calculations, the magnetization shall be reduced to $0.9 \cdot 10^6$ A/m. For this magnetization value, we had also plotted the remagnetization curve (Figure 3, *b*, green curve).

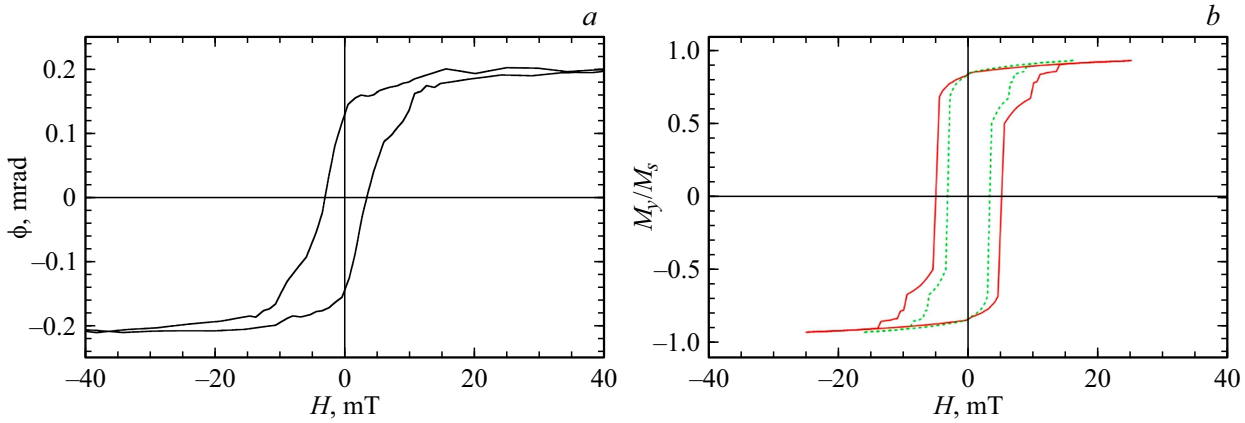

Figure 3. *a* — experimental magnetization curve of the micromagnet array measured by the polarization rotation angle; *b* — remagnetization curve of the micromagnet calculated by the micromagnet simulation method.

The hysteresis loop width for it is 6.5 mT, which is close to the experimental data.

The two abovementioned factors suggest that the actual saturation magnetization of micromagnets is within $0.9-1.4 \cdot 10^6$ A/m. To find its precise value, measure the magnetization of initial Co films by direct magnetometrical methods using a vibration or SQUID magnetometer.

Tow segments may be clearly outlined both on the experimental and simulated curve. The first segment is sudden change in magnetization attributed to remagnetization of the „body“ two micromagnet strips and the second plateau of the loop caused by further gradual remagnetization of the bridge and transformation of inhomogeneous magnetic states near the micromagnet strip ends into the homogeneous state.

To study the scattering fields occurring in the micromagnet gap, magnetic-force measurements were performed. Micromagnet strip widths was 800 nm, and the gap width was 350 nm. Preliminary measurements have shown that the given micromagnets are in the inhomogeneous magnetic state without the magnetic field. Therefore further experimental MFM investigations whose findings will be discussed below were conducted in the magnetizing external field of 0.1 T oriented along the micromagnet strips. This value exceeds the magnetizing field measured by the magnetooptical method. It is a priori lower than the work field of a qubit which is equal to 0.6 T and where the specimen a priori will be in the homogeneously saturated state. The findings are shown in Figure 4: SEM image and MFM contrast of the corresponding segment of the test structure near the gap.

The MFM image clearly shows two poles corresponding to the gap edges and two weaker poles corresponding to the edges of the bridge connecting the micromagnet strips (Figure 4, *b*).

For detailed investigation of the magnetic field gradient distribution along the gap, a series of longitudinal cross-sections of the obtained MFM image was plotted. MFM contrast distributions on the gap edges and in the center were investigated. Lines in Figure 4, *b* show the MFM contrast cross-section positions. The cross-section curves are shown in Figure 4, *d*. Colors of the lines and curves in Figure 4, *b* and *d* correspond to each other.

The obtained curves show that the MFM contrast varies along the gap. The minimum value is near the open edge and grows when approaching the bridge (Figure 4, *d*). The value from the minimum to the maximum MFM signal at different gap edges (red and purple curves in Figure 4, *d*) is about 30%. Such magnetic field gradient is suitable for EDSR implementation in one or more QD.

Colored lines in Figure 4, *b* correspond to cross-sections along which MFM signal distribution is shown in Figure 4, *d*. Experimentally measured MFM contrast cross-sections near the free edge (red dashed and dotted curve), in the center (green dashed curve) and at the edge with the bridge (purple solid curve).

Simulation was performed to interpret the experimental findings and understand the possible way for optimization of the micromagnet design. The micromagnet methods were used to investigate the magnetization distributions in micromagnets in zero and external magnetic fields. Figure 5 shows numerically calculated magnetization distributions and the corresponding MFM images for the system segment in the gap area. The simulation results for the zero external field are shown in Figure 5, *a, b*. Figure 5, *a* shows that inhomogeneous magnetization distributions occur near the micromagnet gap without the external field. This is explained by the fact that such magnetic distributions minimize the magnetostatic energy of the system. Such inhomogeneities result in MFM image smearing and appearance of additional weak poles (Figure 5, *b*).

Figure 5, *c, d* shows magnetization distributions and simulated MFM image in the external field of 120 m oriented along the micromagnet. It can be seen that the system is magnitized homogeneously in the magnetic field. And since this corresponds to the micromagnet utilization in the qubit, all micromagnetic simulation results shown hereinafter were obtained in the saturating external magnetic field of 120 mT.

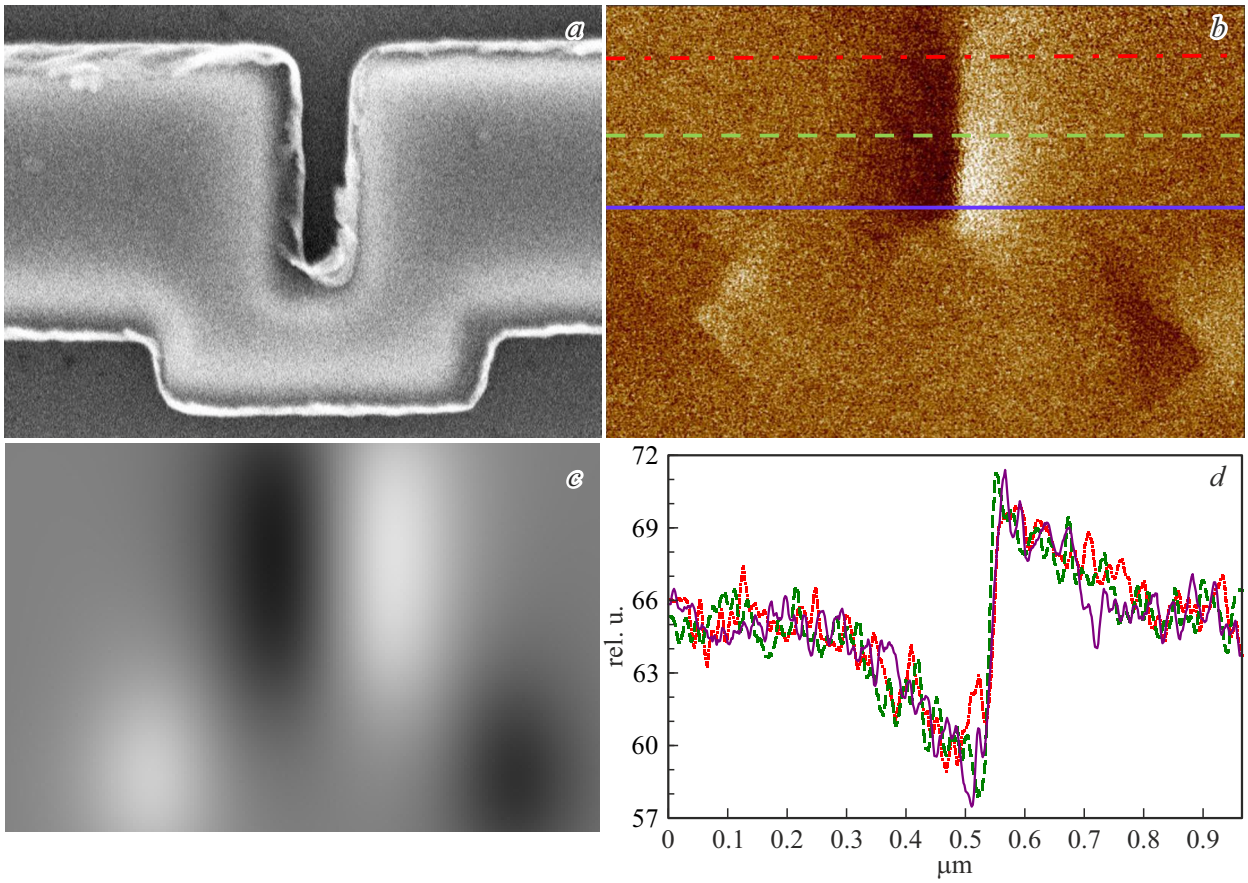

Figure 4. *a* — SEM image of the micromagnet gap, related experimentally measured (*b*) and numerically calculated (*c*) MFM images.

To compare with the theoretical calculations, Figure 4, *b* shows the micromagnet simulation data for the MFM contrast from the micromagnet with the same geometry as in the experiment. Comparison of experimentally measured and numerically calculated MFM contrast cross-sections in the micromagnet gap has shown good agreement between the experimental and simulation data (Figure 4, *b, c*). This suggests that the numerical model is adequate and can be used to calculate magnetic fields in the micromagnet gap for optimization of its parameters and design.

Then this numerical model was also used to calculate the distributions of the magnetic field projections in the system in various directions at a height of 150 nm rom the magnet, which approximately corresponds to the distance from the micromagnet to the place of electron localization (QD formation). The calculations show that the *y*-component of the magnetic field achieves the highest value above the gap. The *z*-component of the field may be much higher, but this field component is localized at the gap edges and bridge ends, the *x*-component of the field is also localized primarily at the bridge ends in the areas with rotated magnetization.

These results show that the simulation is adequate for description of the micromagnet properties. Therefore we used this model for further optimization of the micromagnet design. Micromagnet optimization was previously discussed in [17–21].

When optimizing the magnet geometry, a compromise between the high response rate of the qubit and minimum electric noise sensitivity of the formed qubits is sought. The response rate grows with the Rabi frequency that in turn is proportional to $b_{coup}(x,y) = \sqrt{\left(\frac{dB_x}{dy}\right)^2 + \left(\frac{dB_z}{dy}\right)^2}$. Thus, the response rate is proportional to the magnetic field gradient along the y axis. It is assumed that bcoup has its acceptable values in range from several tenths of mT/nm to 1 mT/nm [21]. The spin dephasing time is inversely proportional to other magnetic field gradients.

$$b_{deph} = \max\left(\left|\frac{dB_y}{dx}\right|, \left|\frac{dB_y}{dy}\right|\right),$$

this allows the relation of dephasing time to the qubit switching time proportional to b_{coup}/b_{deph} to be optimized.

Also, one of the required qubit operation conditions is the magnetic field difference $\Delta B_y > 5$ mT in two neighboring qubits placed in the same micromagnet gap and spaced 100 nm apart. Thus, the resonance frequencies can be separated for two qubits placed within the gap of one mi-

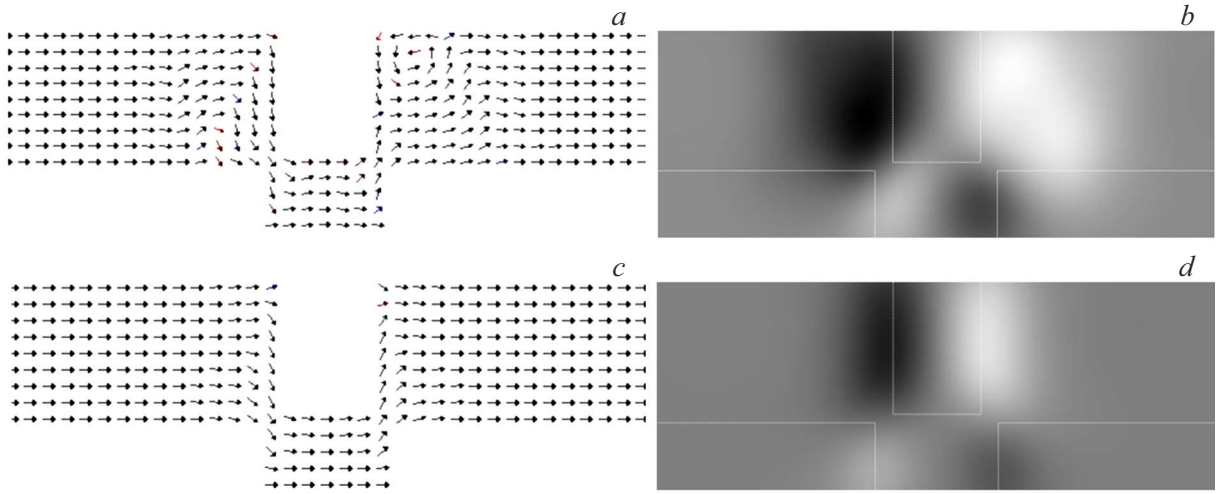

Figure 5. a — magnetization distribution in plane (x, y) without an external field; b —corresponding MFM image; c — magnetization distribution in plane (x, y) in the external field 120 mT; d — corresponding MFM image.

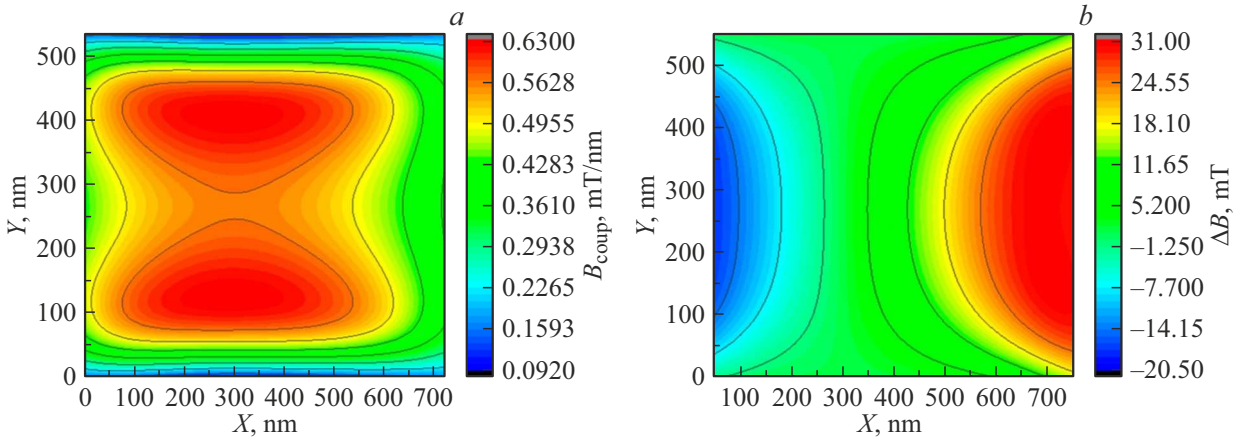

Figure 6. Distribution of b_{coup} (a) and ΔB_y (b) calculated in the micromagnet gap.

cromagnet (Figure 1). Moreover, magnetic field distribution in the system shall be stable to lithography errors.

Taking into account these requirements, parameters of a micromagnet with a Co layer thickness of 200 nm and a gap of 550 × 740 nm were calculated. The micromagnet parameters were selected in accordance with the abovementioned experimental findings achieved for the test micromagnets and the micromagnet property simulation. When choosing the micromagnet parameters, findings of [21] were considered. Micromagnet simulation in this study also used the Landau–Lifshitz–Hilbert equation for the field calculations and showed that micromagnets with low gap width (about 300 nm) have large field gradients (high b_{coup}), but also large spurious gradients resulting in qubit decoherence. Moreover, the magnets with small gap are more sensitive to alignment errors. However, magnets with a gap of 600 nm may have spurious gradients and noise lower by 3 orders of magnitude and they are less sensitive to alignment errors [21].

We calculated two-dimensional distributions of b_{coup} (Figure 6, a) and gradients ΔB_y (Figure 6, b) above the micromagnet gap. According to the calculations, the micromagnet with the chosen parameters provides much higher gradients in the gap center for the magnetic field perpendicular to the y axis, bcoup is 0.55 mT/nm (Figure 6, a). This value shall ensure quite high (5–10 MHz) Rabi frequencies for qubits and low sensitivity to noise induced by the micromagnet. According to the calculations, magnetic field variation along the y axis at a distance of 100 nm for the chosen magnet design is $\Delta B_y = 5–10$ mT (Figure 6, b). This value will be sufficient for the targeted control of two qubits spaced 100 nm apart within the micromagnet gap (difference in the EDSR frequencies for qubits with such spacing will be more than 100 MHz). The proposed micromagnet design is also stable to the manufacturing errors (with alignment accuracy of 50 nm with respect to the QD location) and may be combined with the developed technique of qubit formation in Si/SiGe-epitaxial heterostructures.

Conclusion

Experimental and theoretical studies of the cobalt film micromagnet properties have been performed to find the best micromagnet parameters and design to be used for formation of qubits on Si/SiGe-epitaxial heterostructures. The optical magnetometry methods have been used to plot the magnetization curve of the micromagnet array. A difference has been found between the magnetization curves obtained experimentally and by numerical simulation using the bulk cobalt parameters. The differences may be attributed to defects in the geometrical shape of micromagnets or the difference between the Co film properties and bulk material properties.

The MFM methods were used to measure the spatial distribution of the magnetic field in the gap of the tested micromagnets in the form of relation of the second derivative of the field. The experimental distribution is in good agreement with the simulation results.

Using the calculations of the magnetic field distribution for micromagnets, the Landau–Lifshitz–Hilbert model defined the micromagnet parameters that may provide high (at 5–10 MHz) Rabi frequencies and high phase coherency times for qubits formed on Si/SiGe EH due to low micromagnet-induced noise.

Funding

This study was carried out under the state assignment of the Institute of Applied Physics, Russian Academy of Sciences. Magnets were formed using the equipment provided by the Shared Research Facility „Nanostructures“ (Institute of Semiconductor Physics, Siberian Branch, Russian Academy of Sciences).

Conflict of interest

The authors declare that they have no conflict of interest.

References

[1] Y. Kim, A. Eddins, S. Anand, K.X. Wei, E. van den Berg, S. Rosenblatt, H. Nayfeh, Y. Wu, M. Zaletel, K. Temme, A. Kandala. Nature, 618, 500 (2023). DOI:10.1038/s41586-023-06096-3

[2] Electronic media. Available at: https://www.hpcwire.com/off-the-wire/ionq-unveils-forte-enterprise-and-tempo-rack-mounted-enterprise-grade-quantum-computers-for-data-center-environments

[3] Electronic media. Available at: https://atom-computing.com

[4] Electronic media. Available at: https://www.hpcwire.com/2023/12/07/quantum-market-though-small-will- grow-22-and-hit-1-5b-in-2026/

[5] N. de Leon, K.M. Itoh, D. Kim, K.K. Mehta, T.E. Northup, H. Paik, B.S. Palmer, N. Samarth, S. Sangtawesin, D.W. Steuerman. Science, 372, eabb282 (2021). DOI:10.1126/science.abb2823

[6] P. Stano, D. Loss. *Review of Performance Metrics of Spin Qubits in Gated Semiconducting Nanostructures* https://arxiv.org/abs/2107.06485

[7] A. Noiri, K. Takeda, T. Nakajima, T. Kobayashi, A. Sammak, G. Scappucci, S. Tarucha. Nature, **601**, 338 (2022). DOI:10.1038/s41586-021-04182-y

[8] X. Xue, M. Russ, N. Samkharadze, B. Undseth, A. Sammak, G. Scappucci, L.M.K. Vandersypen. Nature, **601**, 343 (2022). DOI:10.1038/s41586-021-04273-w

[9] M.T. Mądzik, S. Asaad, A. Youssry, B. Joecker, K.M. Rudinger, E. Nielsen, K.C. Young, T.J. Proctor, A. Baczewski, A. Laucht, V. Schmitt, F.E. Hudson, K.M. Itoh, A.M. Jakob, B.C. Johnson, D.N. Jamieson, A.S. Dzurak, Ch. Ferrie, R. Blume-Kohout, A. Morello. Nature, **601**, 348 (2022). DOI:10.1038/s41586-021-04292-7

[10] F. Borsoi et al., Nat. Nanotechnol., 2023. https://doi.org/10.1038/s41565-023-01491-3

[11] A.M.J. Zwerver, T.S. Krähenmann, T.F. Watson, L. Lampert, H. George, R. Pillarisetty, S.A. Bojarski, P. Amin, S. Amitonov, J.M. Boter, R. Caudillo, D. Correas-Serrano, J.P. Dehollain, G. Droulers, E.M. Henry, R. Kotlyar, M. Lodari, F. Lüthi, D.J. Michalak, B.K. Mueller, S. Neyens, J.M. Roberts, N. Samkharadze, G. Zheng, O.K. Zietz, G. Scappucci, M. Veldhorst, L.M.K. Vandersypen, J.S. Clarke. Nature Electron., **5** (3), 184 (2022). DOI:10.1038/s41928-022-00727-9

[12] M. De Michielis, E. Ferraro, E. Prati, L. Hutin, B. Bertrand, E. Charbon, D.J. Ibberson, M.F. Gonzalez-Zalba. J. Phys. D: Appl. Phys., **56** (36), 363001 (2023). DOI:10.1088/1361-6463/acd8c7

[13] Electronic media. Available at: https://www.hpcwire.com/2023/06/15/intel-debuts-tunnel-falls-quantum -chip-and-lqc-program-to-work-with-it

[14] G. Burkard, Th.D. Ladd, A. Pan, J.M. Nichol, J.R. Petta. Rev. Mod. Phys., **95**, 025003 (2023). https://doi.org/10.1103/RevModPhys.95.025003

[15] A. Hollmann. *Relaxation and Decoherence of a 28Si/SiGe Spin Qubit with Large Valley Splitting* (Dissertation, RWTH Aachen University, 2019)

[16] V.L. Mironov. *Osnovy skaniruyushchei zondovoi mikroskopii* (Tekhnosfera,M., 2004) (in Russian)

[17] J. Yoneda, K. Takeda, T. Otsuka, T. Nakajima, M.R. Delbecq, G. Allison, T. Honda, T. Kodera, Sh. Oda, Y. Hoshi, N. Usami, K.M. Itoh, S. Tarucha. Nature Nanotechnol., **13**, 102 (2018).

[18] A. Vansteenkiste, J. Leliaert, M. Dvornik, M. Helsen, F. Garcia-Sanchez, B. Van Waeyenberge. AIP Adv., **4**, 107133 (2014). https://doi.org/10.1063/1.4899186

[19] J. Yoneda, T. Otsuka, T. Takakura, M. Pioro-Ladriére, R. Brunner, H. Lu, T. Nakajima, T. Obata, A. Noiri, Ch.J. Palmstrøm, A.C. Gossard, S. Tarucha. Appl. Phys. Express, **8**, 084401 (2015).

[20] R. Neumann, L.R. Schreiber. J. Appl. Phys., **117**, 193903 (2015).

[21] N.I. Dumoulin Stuyck, F.A. Mohiyaddin, R. Li, M. Heyns, B. Govoreanu, I.P. Radu. Appl. Phys. Lett., **119**, 094001 (2021). https://doi.org/10.1063/5.0059939

Translated by E.Ilinskaya